# An Inkjet-Printed Field-Effect Transistor for Label-Free Biosensing

*Mariana Medina-Sánchez, Carme Martínez-Domingo, Eloi Ramon, and Arben Merkoçi**

**A flexible, biological field-effect transistor (BioFET) for use in biosensing is reported. The BioFET is based on an organic thin-film transistor (OTFT) fabricated mainly by inkjet printing and subsequently functionalized with antibodies for protein recognition. The BioFET is assessed for label-free detection of a model protein, human immunoglobulin G (HIgG). It is characterized electrically to evaluate the contribution of each step in the functionalization of the OTFT and to detect the presence of the target protein. The fabrication, structure, materials optimization, electrical characteristics, and functionality of the starting OTFT and final BioFET are also discussed. Different materials are evaluated for the top insulator layer, with the aim of protecting the lower layers from the electrolyte and preserving the BioFET electrical performance.**

## 1. Introduction

Thin-film transistors (TFTs) are powerful devices in semiconductor manufacturing and form the basis of countless electronic devices, such as memory chips,[1] photovoltaic cells,[2] logic gates,[3] and sensors.[4] Most contemporary TFTs are based on inorganic materials (mainly silicon). An interesting alternative to inorganic TFTs is organic TFTs (OTFTs), which offer the possibility of mass production by using the conventional printing technology and working with low-cost materials, resulting in an especially good approach to obtain functional and easy-handling devices; however, numerous inherent problems still remain, especially concerning the long-term stability and lack of reliability, that require further studies and standardization before devices can be fully applied in field applications. OTFTs are amenable to the use of multiple substrates and can operate at room temperature. They are especially interesting in biological applications, as they enable the use of a wide range of biocompatible and biodegradable materials detecting a wide range of analytes, including gases (such as $NH_3$ and $NO_2$), proteins, DNA, bacteria, etc.[5] However, the performance of these devices is limited by low sensitivity (around several micrograms per milliliter). Large surface-to-volume ratio nanostructures, high-*k* dielectrics,[6] or 1D materials such as silicon nanowires, carbon nanotubes,[7,8] and graphene have been used to enhance the sensitivity. Despite this fact, their fabrication has limitations, requiring sophisticated fabrication techniques to precisely deposit them. Solution-processed inorganic thin-film devices may be promising; nevertheless, organic semiconductors benefit from relatively low temperature, solution processing capability, and the flexibility to work on any kind of substrate, with a high mobility.[9] Regardless of the organic high-performance materials, the limit of detection can be improved by means of: i) different geometries of the OTFT, and, ii) performing detection under the sub-threshold region.[10]

Advances in organic electronics have yielded diverse, low-cost electronic components that have enabled the development of thin, flexible, and environmental friendly devices.[11] Unlike traditional inorganic TFTs, which are made by a complicated photolithography processes that requires expensive masks and cleanroom facilities, OTFTs can be easily fabricated by inkjet printing and do not require cleanroom settings. Nevertheless, contemporary OTFTs suffer from certain drawbacks that researchers are currently endeavoring to overcome: high operating voltages, low material stability, and relatively short operating lifetimes.

Among the OTFT-based devices, organic field-effect transistors (OFETs) have been selected over organic electrochemical transistors (OECTs) for sensing purposes. The main factors motivating this choice are: i) dielectric functionalization without losing electrical properties of the organic semiconductors, and, ii) reusability device since the transduction mechanism is based on electrostatic gating consisting on a capacitive coupling between the organic semiconductor and the gate in contrast of the electrochemical doping/de-doping mechanism

M. Medina-Sánchez,[+] C. Martínez-Domingo,[+]
Prof. A. Merkoçi
Nanobioelectronics and Biosensor Group
Institut Català de Nanociència i Nanotecnologia (ICN2)
Campus de la UAB
08193, Bellaterra, Barcelona, Spain
E-mail: arben.merkoci@icn.cat
M. Medina-Sánchez
Institute of Integrative Nanosciences (IIN)
Leibniz Institute for Solid State and Materials Research
Dresden, Germany
E. Ramon
Universitat Autònoma de Barcelona
Campus de la UAB
08193, Bellaterra, Barcelona, Spain
E. Ramon
Institut de Microelectrònica de Barcelona
IMB-CNM (CSIC). Campus de la
UAB 08193, Bellaterra, Barcelona, Spain
Prof. A. Merkoçi
Institució Catalana de Recerca i Estudis Avançats (ICREA)
08193, Bellaterra, Barcelona, Spain
[+]These authors contributed equally to this work.

**DOI: 10.1002/adfm.201401180**

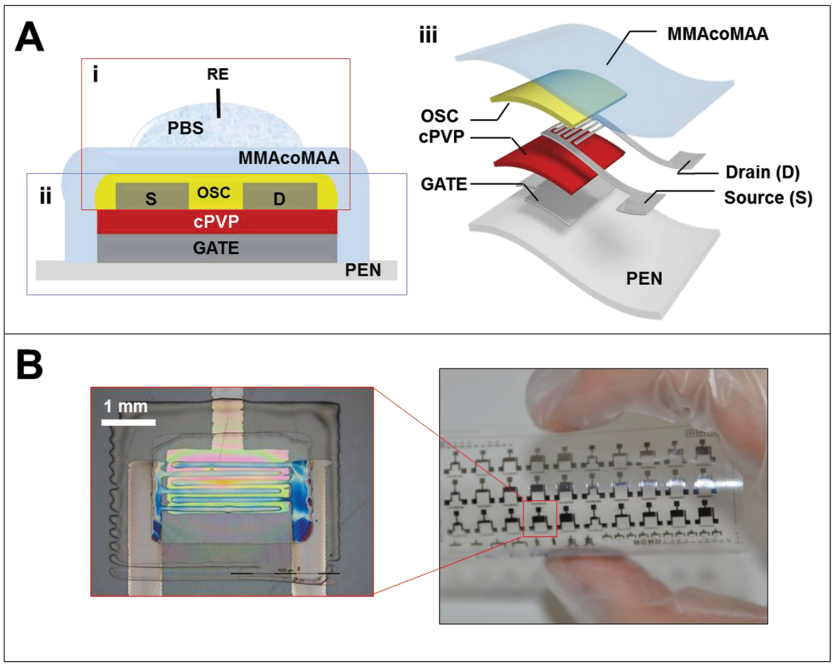


**Figure 1.** A) Structure of the BioFET: i) the top OFET; ii) the bottom OFET, and, iii) each layer of the BioFET. The OFET channel dimensions (*W*: channel width; *L*: channel length; in μm) were: $W \times L = 20\,000 \times 40$ or $40\,000 \times 40$. FS0027: p-type organic semiconductor; MMAcoMAA: methyl methacrylate copolymer: PEN: polyethylene-naphthalate; cPVP: cross-linked poly-4-vinylphenol; and RE: reference electrode (platinum wire). B) Photographs of the printed OFETs.

of OECTs.[12,13] Over the past few years, a type of OFET called the biological field-effect transistor (BioFETs) has garnered major interest for use in biosensing. There are two primary differences between standard OFETs and BioFETs: firstly, where the former has a gate contact, there latter contains an electrolyte and a reference electrode that together yield an electrolyte–insulator–semiconductor field-effect transistor (EISFET) structure[14]; secondly, the insulator in a BioFET is functionalized with biological materials that enable specific recognition of the target analyte.[15] To date, BioFETs have been fabricated by diverse processes that imply assembly of many functional materials, making them expensive and time-consuming. However, the production of OTFTs in general has recently advanced to levels of high throughput and integration, thanks not only to conventional methods, but also to printing technologies. Consequently, Organic electronics are ideal candidates for sensing applications in which low-cost and disposable devices can be fabricated with accurate results.[16] BioFETs for electrochemical detection of cancer biomarkers (e.g., interleukin-6) in serum, based on gold electrodes that are inkjet-printed onto a polyimide (PI) substrate,[17] and for glucose detection via sensing of hydrogen peroxide, made from a polymer mixture of two ionomers such as poly (3,4-ethylenedioxythiophene) and poly(styrene sulfonic acid),[18] have been reported.

Myriad techniques have been explored for deposition of organic materials[19] onto a target substrate, including printing (e.g., inkjet,[20] screen,[21] microcontact,[22] flexographic,[23] or laser methods) and nanolithography (e.g., scanning probe microscopy,[24] or photo/e-beam deposition). Inkjet printing has become one of the most promising of these techniques, as it entails rapid, additive manufacturing with small volumes of ink to achieve high pattern precision, resolution, and reproducibility. Furthermore, inkjet printing is better suited for rapid prototyping in research than are technologies that require the use of masks.[25] It can be used to deposit a wide range of materials (electrical, chemical, optical, biological, etc.) of different compositions (soluble liquids, dispersions of micro- or nanoparticles, melts, and blends) and viscosities. Lastly, inkjet printing is amenable to deposition of certain compounds (e.g., conductive and/or semiconducting polymers, and large biomolecules) that can only be deposited using a solution-based technique, as they cannot be deposited by conventional vacuum-deposition techniques.

Among the most important applications for biosensors is medical diagnosis. Researchers are endeavoring to create highly efficient, low-cost, point-of-care biosensors that enable earlier diagnosis (and therefore, faster treatment) of ill patients.[26] The biosensors for this use are typically based on protein-analysis immunoassays, which can require the use of a label[27] or be label-free.[28–30] In the former type, labels such as fluorescent dyes,[31] radioisotopes,[32] or quantum dots[33] are used to indirectly quantify the target protein. In contrast, in label-free immunoassays some inherent property of the primary transducing signal (i.e., the mass, conductivity, or insulator characteristics) is measured.

Herein are reported the design, fabrication, and evaluation of a flexible BioFET for label-free biosensing. The BioFET is based on an inkjet-printed OTFT whose insulator was biofunctionalized with specific antibodies for protein recognition. As proof-of-concept, the resulting BioFET was evaluated for quantification of a model protein, G (HIgG).

## 2. Operating Mechanism

The BioFET reported here, made by functionalizing a previously described OFET with anti-HigG antibodies, ensures the electrical detection of biomolecular interactions between the target protein and the antibody. These interactions occur on the BioFET dielectric through capacitive coupling with the organic semiconductor. A schematic of the BioFET is shown in **Figure 1**A. The structure is a dual-gate OFET that comprises source, drain, and two gates (Figure 1A-i,ii,iii). However, in this BioFET, rather than a top gate contact, there is an electrolyte solution (phosphate buffer saline [PBS]), an antibody–protein conjugate and a reference electrode (Pt wire; 0.2 mm diameter). The accumulated charge on the insulator in the BioFET can lead to a variation in the source–drain current. Since the change in the electrical charge is related to the interaction between the target biological molecules and the semiconductor, the BioFET can be used to monitor this interaction effectively by measuring,

with high sensitivity, the variations in transistor response (*I–V* curves).

The developed BioFET has two main advantages. Firstly, it is easy to miniaturize, making it suitable for future applications involving complex systems. Secondly, and in terms of biosensing, it can be equipped with a bottom OFET for using as test component, to confirm the reliability of the organic semiconductor. In fact, the dual-gate structure could be used for current control (although in the present work, this was not done). Photographs of the printed OTFTs in the BioFET are shown in Figure 1B.

### 2.1. Considerations for the BioFET Fabrication

The BioFET was fabricated by inkjet printing. The printing parameters for printed BioFETs can be tailored to define optimal morphologies according to the intrinsic constraints of the materials. To explain the relationship between layer morphology and electrical performance, one must consider all the variables that affect the transfer characteristics in the saturation regime of an OFET, as shown below in Equation 1:

$$I_{DS} = \mu . C_i . \frac{w}{L} \cdot \frac{(V_G - V_\tau)^2}{2} \quad (1)$$

where $I_{DS}$ is the drain–source current (A); $\mu$ is the field effect mobility ($cm^2 \cdot V^{-1} \cdot s^{-1}$); $C_i$ is the capacitance per unit area of the insulating layer ($F \cdot cm^{-2}$); $W$ is the channel width of the transistor (μm); $L$ is the channel length of the transistor (from source to drain, in the direction of the current flow [μm]); $V_G$ is the gate voltage; and $V\tau$ is the threshold voltage (V), which is the minimum gate voltage required for establishing the conductive channel. Thus, the most important printing parameters are related to the dimensions of the OFET, including the thickness of each layer.

Another important factor in printing is the type of printer used. Drop-on-demand (DoD) piezoelectric printers, such as the one employed in the work reported here, use a piezoelectric transducer to eject the ink droplets. The transducer is actuated by a voltage pulse whose frequency ranges from 1 to 20 kHz (in commercial printers).

The relative distribution of deposited material across the printed geometry can be controlled by tuning certain printing parameters related to temperature or to drop-on-demand delays, such as the temperature of the cartridge or platen (in this work, the temperature of cartridge was disabled),[34] the jetting frequency, the jetting waveform, or the voltage of the print-head nozzles. Other important printer parameters that can be adjusted to achieve better features include drop spacing (DS), the distance between two consecutively printed droplets), which is scaled by the wetting diameter of the droplet on the substrate. The resolution of the final pattern is determined by the drop spacing. The nozzle orifice size of the printer used for all layers was 21.5 μm (corresponding to a 10 pL printhead).

One crucial parameter of the ink itself is its viscosity, as the state of the droplet strongly influences the morphology of the deposited film. Higher viscosities enable better control over droplet spreading, but lower viscosities (range of cPa) are needed to ensure that the print-head nozzles can eject the ink. Ink viscosity is usually adjusted by modifying the solvent or the concentration of the solute in the solvent.

Before the printer is set up, and the ink and printing parameter values are chosen, the substrate must be selected. Albeit the most commonly used materials are glasses or flexible plastics, including polyethylene terephthalate (PET) due to its low cost and polyethylene naphthalate (PEN) for its low surface roughness, a wide variety of substrates, including paper and even biological tissue can be used. PEN and PET roughness were analyzed by atomic force microscopy (AFM). In Table S5 and S6 (showing the properties of these two materials in comparison with others such as PI, PEI, and PSS; see the Supporting Information (SI)) indicate the measured values of root-mean-square (Rms) and average (Ra) roughness for each substrate (PEN and PET).

In this work, PEN substrate is used due to its many convenient properties such as strength, heat resistance, and dimensional stability, among others. This material is specially appropriated for printed electronics, since it has a pretreated smooth surface with a roughness around 0.82 nm, being in the range of silicon wafers surface roughness.

Finally, the drying of the ink onto the substrate is also important—namely, the physical and chemical interactions between the ink solution and the substrate during evaporation. This factor is especially important when there is a recirculation flow (induced by a Marangoni flow effect) opposite to the convective flow,[35] a scenario which is the leading cause of the so-called "coffee ring effect" Both bottom gate and drain and source electrodes show a low coffee ring effect while the cross linker cross-linked poly-4-vinylphenol (cPVP) presents a clear accumulation of the material at the edges. Figure S1 shows the profile of the Ag bottom gate, bottom cPVP, drain, and source electrodes and FS0027 organic semiconductor respectively. Both bottom gate and drain and source electrodes show a low coffee-ring effect while the cPVP presents a clear accumulation of the material at the edges.

### 2.2. Characterization of the Insulator Layer

As previously explained, the fabricated BioFET comprises a dual-gate OTFT structure. In previous work by Ramon et al.,[36] the structure of the OTFT was optimized and its constituent materials were tested. The conductive layers are made of silver nanoparticles, the insulator layer is made from cPVP, and the semiconductor layer is made of the amorphous *p*-type polymer FS0027. However, for most biosensing applications that use BioFETs, the top insulator film should also act as a coating layer to protect the device, since it is in contact with an aqueous solution. In the BioFET reported here, silver nanoparticles were used for the source and drain contacts. Since silver nanoparticles are electrocatalytic in aqueous media,[37] it is very important to insulate the source and drain contacts from the electrolyte. Insulator had to be analyzed for such purpose.

Various materials were explored for the top insulator (i.e., the insulating interface between the semiconductor and the electrolyte). The first studied material was cPVP, which offers good printability and insulation for an OTFT. However, cPVP

dissolves in aqueous media,[38] consequently a fast decomposition reaction was triggered upon application of a sweep voltage in the electrolyte. cPVP is not stable during the conjugation steps due to its poor resistance to the humidity; however, cPVP can support electrical field of up to 0.3 MV $cm^{-1}$ in dry environments (Figures S2A,B in the SI). A simple test for the insulator material pre-selection was done, which has to be biocompatible, amenable to use in the desired BioFET, easy to process and suitable for mass-production. A schematic of the metal–insulator–electrolyte (MIE) structure used to characterize the different insulator materials is shown in Figure S3A.

The next three materials separately evaluated for the top insulator layer were Norland Optical Adhesive (NOA) 68, a polyester resin and polymethyl methacrylate (PMMA). Each one was deposited onto the silver contact, and then put into contact with the electrolyte. A voltage sweep (0 to –20 V) was applied, and the surface characteristics of each material were studied by optical microscopy and by current measurements. In all three cases application of the voltage led to soft breakdown produced by many pinholes between the reference electrode and the silver contact, which led to high current density and consequently, to a total loss of insulation (Figures S3B,C, and D). Therefore, all three of these materials were ruled out.

The last material evaluated as possible top insulator was MMAcoMAA (methyl methacrylate copolymer methacrylic acid). Despite never having been reported as an insulator for organic electronics, MMAcoMAA and related compounds form the basis of many positive resists. They are distinguished by their high-resolution features, strong adhesion to metallic or semiconducting supports, and good resistance to solvents and reagents. Thus, MMAcoMAA was subjected to various electrical measurements (capacitance, resistance, and current) with the objective to characterize its electrical behavior and determine its constraints—namely, in terms of achieving the lowest current leakage and the greatest resistance to the aqueous medium possible.

Once MMAcoMAA had been chosen as the material for the top insulator in the BioFET, two additional factors were optimized: the number and thickness of the layers to be used. Current–voltage (*I*–*V*) measurements were taken by applying a bias voltage to the top of the MIE structure, using aq. KCl (0.1 M) as electrolyte. The current density plot for different numbers of layers, and different layer thickness values, is shown in **Figure 2**. The best results were obtained for one layer of 1.5 µm thickness. Thus, a layer of MMAcoMAA was chosen as the top insulator in the BioFET.

### 2.3. SEM Characterization of Each Layer in the BioFET

The morphology of each layer in the BioFET was characterized by optical microscopy and by scanning electron microscopy (SEM). **Figure 3**A and B show optical microscopy images of the top view of each layer (top row) and SEM images of the cross-section for each layer (bottom row), the latter of which were used to measure the real thickness of each layer: i) the bottom gate, based on silver nanoparticle ink (thickness: 573 nm); ii) the bottom insulator, made of cPVP (thickness: 650 nm); iii) the source and drain contacts, printed with silver nanoparticle ink (thickness: 328 nm; note: due to the wettability of the cPVP, this layer is thinner than the silver bottom-gate); iv) the (*p*-type) semiconductor, FS0027 (thickness: ca. 300 nm); and, finally, v) the top MMAcoMAA insulator (thickness: 1.5 µm). Figure 3C shows a SEM image of a focused ion beam (FIB) cross-section of the BioFET (cutting dimensions: 200 × 10 × 8 $\mu m^3$) that had been subjected to an extra polishing step to maximize image quality.

### 2.4. Electrical Characterization of the OFET

In any transistor, the control of the electrons or holes from source to drain depends on the size and shape of the channel and on the applied gate voltage. When *p*-channel devices are in *accumulation mode*, the applied voltage between gate and source (negative) produces an accumulation region in which the channel is formed by the charge carrier that is produced in the gate insulator/semiconductor interface, thereby enabling the current to flow (ON state). In contrast, when the device is in *depletion mode*, the applied voltage between gate and source (positive) closes the channel, increasing the resistance from source and drain and consequently, stopping the flow of current (OFF state). In *n*-channel devices, the positive voltage attracts electrons toward the gate, forming a conductive channel. The voltage necessary to open the conduction channel is known as the *threshold voltage* ($V\tau$).[39] Most OTFTs operate in accumulation mode, whereas most inorganic TFTs operate

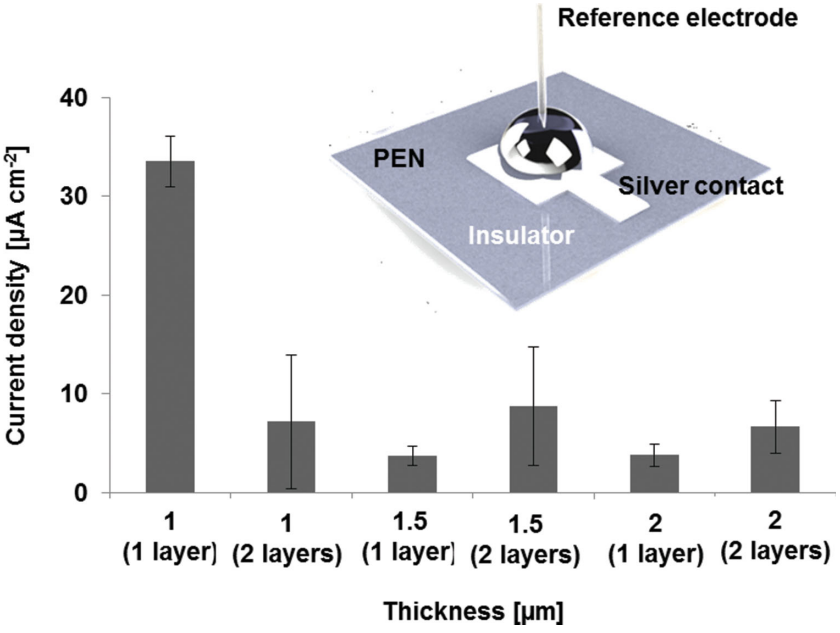


**Figure 2.** Electrical characterization of MMAcoMAA insulator layers according to the number and thickness of each: current density measurements at –30 V.

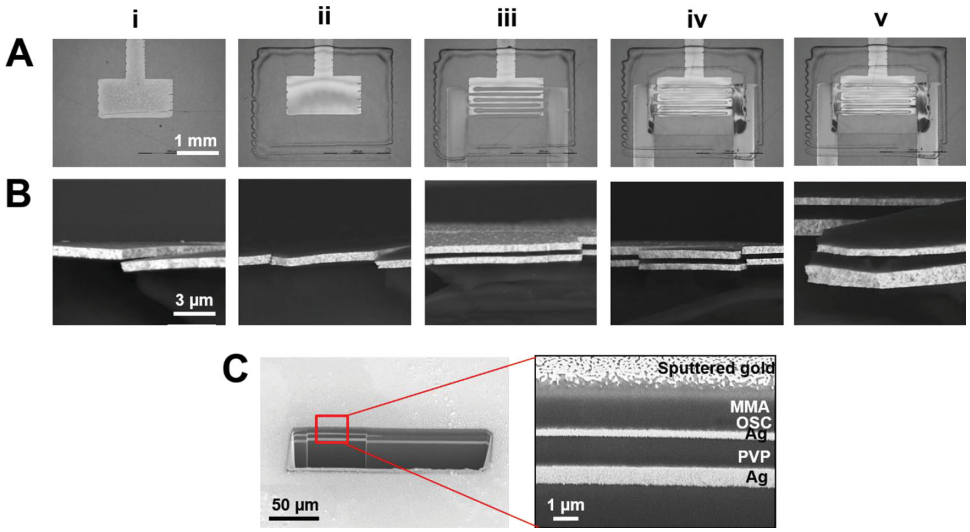


**Figure 3.** A) Optical microscopy images of each layer in the BioFET: i) bottom gate (silver nanoparticle ink); ii) bottom insulator (cPVP); iii) source and drain contacts (silver nanoparticle ink); iv) *p*-type organic semiconductor (FS0027); and, v) top insulator (MMAcoMAA). B) SEM image of an FIB section of the BioFET (inset: zoom). All the SEM images were acquired in backscattering mode.

in inversion mode. Conductance occurs in the ON state, due to the layer of charge carriers that are formed in the semiconductor within a few angstroms from the gate insulator/semiconductor interface, and only upon application of a suitable $V_G$. Thereby, OTFTs operate through the creation and elimination of a thin layer of charge carriers at the gate insulator/semiconductor interface.

In order to have an approach of the leakage process of the bottom OFET, we fabricated a simple device consisting of a metal–insulator–metal (MIM) capacitor. All experimental conditions such as the material, printing parameters, and post-treatment of the cPVP are exactly the same as those for the BioFET fabrication. This dielectric withstands an electric field of 0.3 MV $cm^{-1}$ with a current density of 8 nA $cm^{-2}$, moreover, the degradation of the dielectric upon bias stress is not observed.

Some interesting high-performance semiconductors, including 6,13-*bis*(triisopropylsilylethylthynyl) pentacene (TIPS-pentacene), amorphous polymer FS0087 provided by Flexink Inc. among others, were tested. In terms of morphology, these mentioned semiconductors lacks of homogenous surface basically due to high crystallization while deposited by inkjet printing technology.[40–42] In terms of electrical behavior, high motilities and low threshold voltage were reached thanks to the use of fluoropolymer[43] dielectrics but they are very hydrophobic and require conventional techniques for their biofunctionalization. TIPS-pentacene (commercially available) was discarded since (i) it is not appropriate when high-temperatures are required in the materials deposited on top because it suffers destructive structural changes when the temperature is higher than 120 °C; since we bake MMAcoMAA material at 150 °C after the semiconductor deposition, we would be cracking and losing electrical properties of the semiconductor placed on the bottom; (ii) formation of very rough films surfaces due to the crystallization when inkjet printing technique is applied using both 1% wt. in chlorobenzene and 3% wt in anisole as solvent[44,45] (see Figure S8 and S9 in the SI). Finally, FS0027 was selected for its stability along the time, good printed morphology and low threshold voltage.

Since the electrical properties are essentially determined by the interface between the dielectric and the semiconductor, a metal–insulator–semiconductor (MIS) structure was fabricated using the same materials, printing conditions, and post-treatment (as for BioFET fabrication). MIS devices are very promising because they can provide valuable information about the quality of the dielectric/semiconductor interface. The MIS capacitors where also characterized by using small signal impedance techniques mainly, capacitance–voltage (*C*–*V*). The electrical characterization shown in Figure S10 reveals that both accumulation and depletion regions can be established. The voltage at which the accumulation region starts is –0.9 V and indicates that there is not a deep trapping phenomenon in the interface dielectric/semiconductor.

**Figure 4**A, and B shows the transfer and the output plot for the OFET without electrolyte (i.e., the bottom OFET). For this technology, $V\tau$ is ca. –3.5 V, and the mobility is $2.5 \times 10^{-4}$ $cm^2 \cdot V^{-1} \cdot s^{-1}$ with a deviation of 0.7 V and 0.3 $cm^2 \cdot V^{-1} \cdot s^{-1}$, and a current on/off ratio of 200. A current of 0.4 µA at $V_{DS} = -30$ V for a transistor of 40 µm of channel length and 10 mm of channel width ($W/L$ ratio of 250) is achieved.

The electrical characteristics for each OFET as a function of the bending radius were determined with a convex direction radii $R$ of approximately 1.4, 1.6, 2.8, 3.5, and 5.5 mm, corresponding to strains ($S$) of approximately 4.5%, 4%, 2.2%, 1.8%, and 1.1%, respectively ($S = d/2R$, where $d$ is the thickness of the substrate); thus, for higher values of $S$, the bending curvature is lower. Figures 4C and D show the transfer characteristics and the mobility of the OFET as a function of bending radius. Before bending, good average mobility was observed according to our technology. As the strain induced increases, the mobility on the interface cPVP–semiconductor decreases approximately 90% (from $1.64 \times 10^{-4}$ to $1.65 \times 10^{-5}$ $cm^2 \cdot V^{-1} \cdot s^{-1}$ for a strain such as 4.5% corresponding to a radius of 1.4 mm. Nevertheless, for low strains from 1.1% up to 4%, the decrease of the

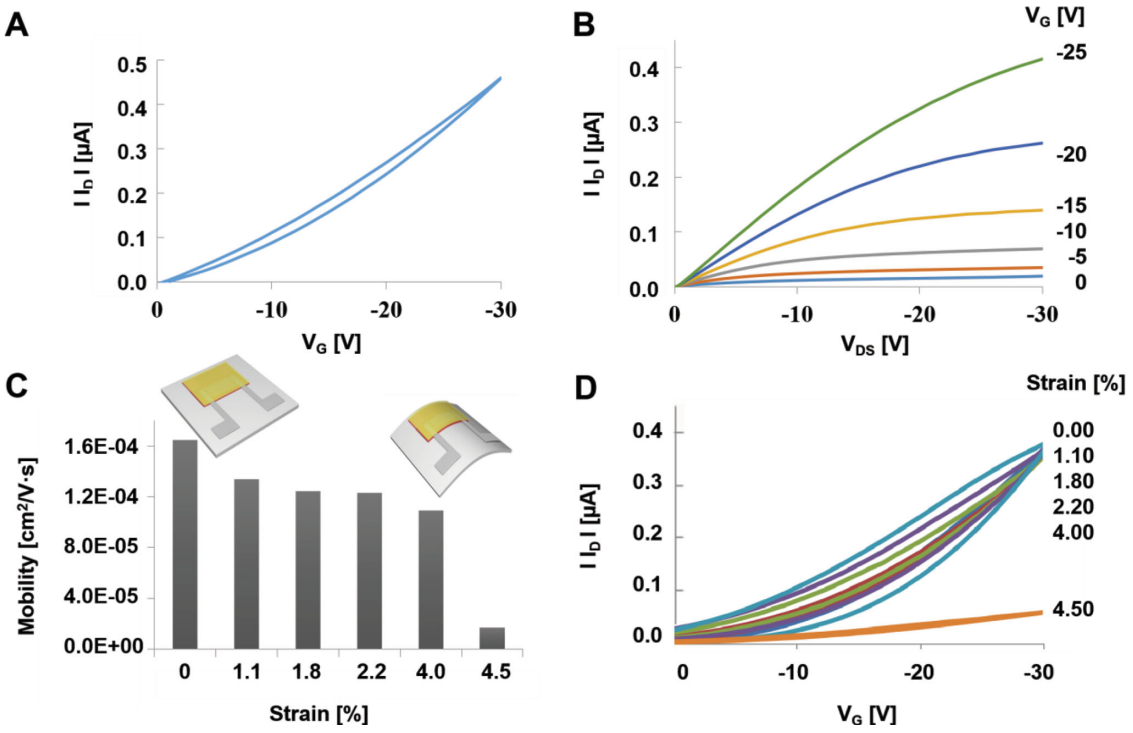


**Figure 4.** Transfer curves for the FS0027 semiconductor layer at room temperature: A) OFET transfer curve in saturation mode ($V_{DS}$ = –30 V), B) OFET output plot for a *W*/*L* ratio of 250, C) mobility of the OFET in function of bending radii, and, D) transfer curve characteristics at different strains.

mobility is not significant. In contrast, the threshold voltage increases approximately 10 V for higher strain values. This result is in accordance with the literature.[46,47]

### 2.5. Functionalization of the MMAcoMAA Surface

The surface of the MMAcoMAA layer was amino-functionalized by treatment with 1% (3-aminopropyl triethoxysilane) APTES. The final surface density of amino groups in the functionalized layer final was 0.18 $\mu M \cdot cm^{-2}$ (**Figure 5**A), as determined by colorimetric quantification with acid orange II dye.

The presence of surface amino groups on the MMAcoMAA layer was confirmed by various methods, including binding of the fluorescent label bovine serum albumin (BSA) labeled with the ALEXA 555 fluorophore to the amino groups and subsequent fluorescence quantification by epifluorescence microscopy (Figure 5B).

Figure S5A shows the change in contact angle of the MMAcoMAA. First, the angle decreased from 74° to 13°, due to the appearance of more-hydrophilic functional groups after the plasma treatment. However, the contact angle increased upon amino-functionalization of the surface, reaching values from 46° to 75°, depending on the concentration of APTES used (0.1%, 1%, 2% or 4%). Finally, the bare and amino-functionalized MMAcoMAA surfaces were each incubated with BSA, and then studied by AFM for changes in phase angle. The greatest change in phase angle was observed in the amino-functionalized MMAcoMAA surface. Although proteins such as BSA can easily attach non-specifically to almost any surface, in this application there was a clear difference between the bare MMAcoMAA surface and the amino-functionalized one (Figure S5B in the SI).

## 3. Label-Free Immunoassay

### 3.1. The EIS

Since the electrolyte–insulator–semiconductor (EIS) structure is a precursor of the BioFET, it was used to evaluate detection of an immobilized model protein, BSA (1 µg $mL^{-1}$), as shown in **Figure 6**A. The EIS comprised, from bottom to top: a conductor (Ag nanoparticle ink); a semiconductor (FS0027); an insulator (MMAcoMAA); an electrolyte (PBS); and a reference electrode (Pt wire). Two EIS structures were tested by *C*–*V* measurements (1 kHz, room temperature): one with an amino-functionalized MMAcoMAA surface and one with a BSA-functionalized MMAcoMAA surface (made by amino-functionalization and subsequent incubation with BSA). This technique enabled quantification of parameters such as surface-state response, surface accumulation, and layer thickness.[48] The *C*–*V* characteristics of the two EISs are shown in Figure 6B-i (amino-functionalized EIS) and Figure 6B-ii (BSA-functionalized EIS). In each case, the capacitance depended on bias voltage and showed two regions of accumulation/depletion, indicating the modulation of the carriers. The capacitance remained constant under forward bias; although above the threshold, it gradually increased to reach the maximum peak value. This phenomenon can be explained by short-circuited parallel capacitance and is based on an RC model circuit. As shown in *C*–*V* plots in Figures 6B, the two configurations differed markedly in their

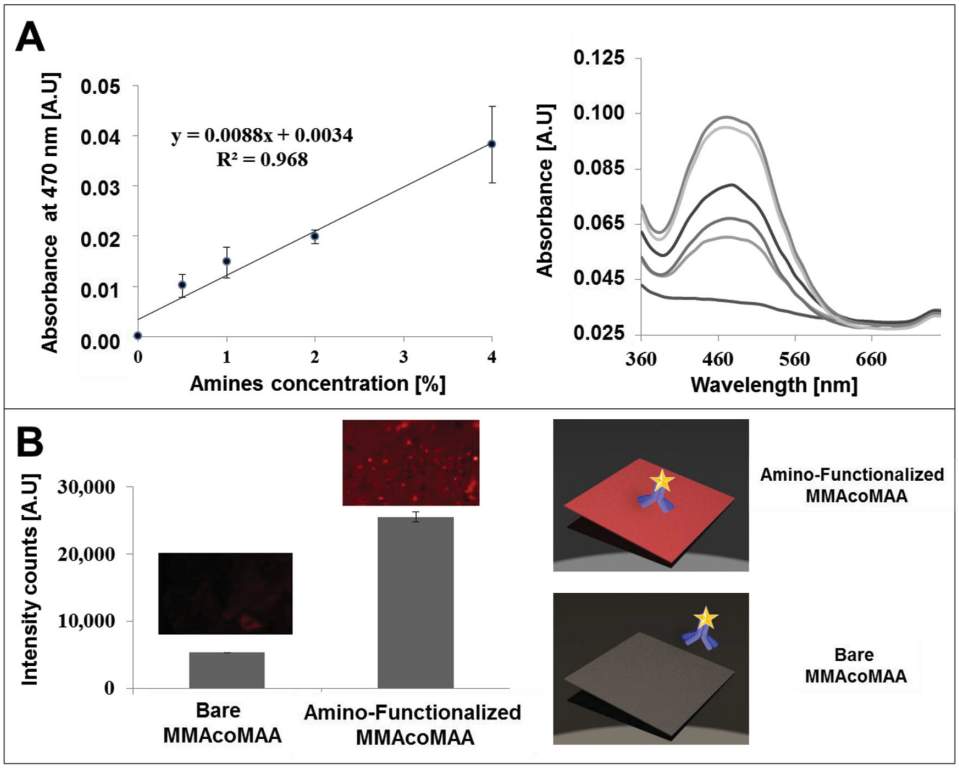


**Figure 5.** Characterization of the amino-functionalized MMAcoMAA insulator surface. A) Absorbance measurements: calibration curve of the surface amino groups (left), and the characteristic absorbance plot (right). B) Fluorescence plot for two MMAcoMAA surfaces (bare and amino-functionalized) labeled with a fluorescent protein.

respective peak heights of capacitance. The capacitance values for the two EIS configurations (280 nF for the amino-functionalized EIS (Figure 6C-i), and 100 nF for the BSA-functionalized EIS (Figure 6C-ii)) were consistent with the aforementioned observations.

### 3.2. Electrochemical Evaluation of the OTFT/BioFET in Three Configurations

The OTFT/BioFET was electrochemically assessed in three configurations. **Figure 7**A shows the schematics for the bottom OTFT (Figure 7A-i): the OTFT with electrolyte (on the MMAcoMAA layer; Figure 7A-ii); and the BioFET (with electrolyte onto the MMAcoMAA layer plus reference electrode; Figure 7A-iii). The last of these corresponds to a BioFET configuration, as the electrolyte is biased by the reference electrode. Figure 7B shows the electrical response for each of these three configurations upon application of the gate voltage. As observed, the transfer characteristic of the device in a dry environment for the bottom OTFT (Figure 7B-i) does not show any significant hysteresis. Due to the requirement of proper operation of the BioFET in wet environments in biosensing applications, Figure 7B-ii shows the electrical response of the OTFT for

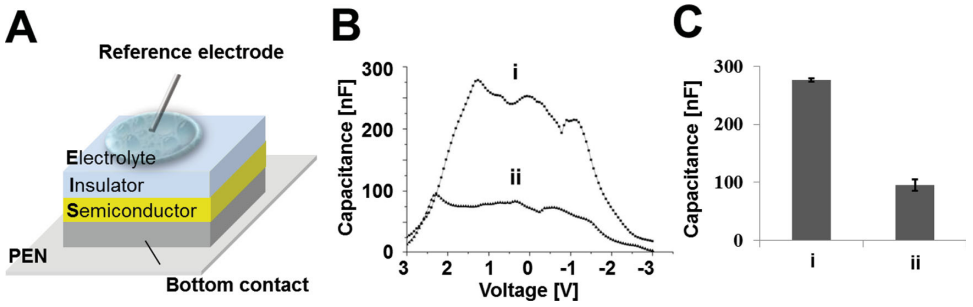


**Figure 6.** A) Schematic of the EIS (from bottom to top): conductor (Ag nanoparticle ink); *p*-type organic semiconductor (FS0027); insulator (MMAcoMAA); electrolyte (PBS, 2 µL); and, reference electrode (Pt wire). B) Capacitance–voltage measurements with electrolyte (PBS) on the EIS in two structures, with: i) amino-functionalized (1% APTES) insulator, or, ii) BSA-functionalized (1 µg $mL^{-1}$) insulator, and C) Capacitance measurements for two different EIS structures, with: i) amino-functionalized insulator, and, ii) BSA-functionalized insulator.

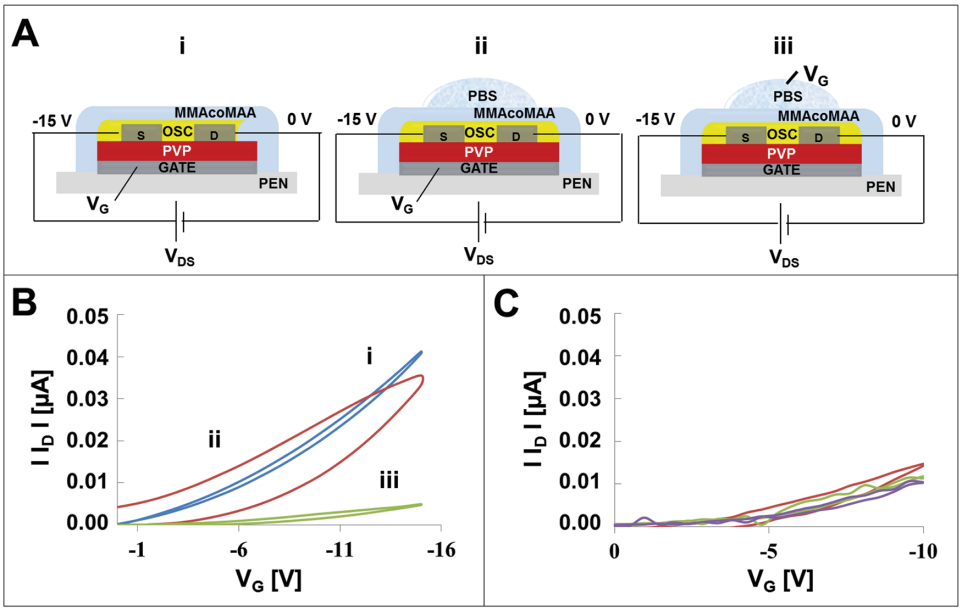


**Figure 7.** A) Schematics for the OTFT in three configurations: i) bottom gate; ii) with electrolyte (on the MMAcoMAA layer); and, iii) with electrolyte (on the MMAcoMAA layer) plus reference electrode. B) The corresponding *I–V* plots for all three configurations. C) Repeatability plot for the third configuration (electrolyte plus reference electrode).

a drop of the electrolyte placed onto the MMAcoMAA using the configuration shown in Figure 7A-ii. In this case, the electrolyte is assumed to induce pronounced hysteresis, thereby increasing the OFF-current and consequently, decreasing the $I_{ON}/I_{OFF}$ ratio. The transfer characteristic for the BioFET (Figure 7B-iii) using the configuration shown in Figure 7A-iii reveals a decrease in current, which is caused by the differences in insulator thickness and in the permittivity between the bottom insulator (cPVP) and the top insulator (MMAcoMAA). Lastly, Figure 7C shows the repeatability of the transfer curve for the BioFET configuration.

Once the BioFET configuration in which an electrolyte was on the top gate had been evaluated, the steps of functionalizing its MMAcoMAA insulator with specific antibodies (**Figure 8**A) were assessed by measuring the change in current after each one. Figure 8B shows the transfer characteristic for each step: i) amino-functionalization (with 1% APTES); ii) immobilization of the capture antibodies; iii) blocking to prevent non-specific absorption; and, iv) analyte conjugation. Figure 8B-i shows the *I–V* curve for the amino-functionalized MMAcoMAA surface. Immobilization of the antibodies onto the surface led to a slight decrease in current (Figure 8B-ii); blocking of the surface with buffer (PBS supplemented with casein and tween) led to another, albeit negligible, decrease (Figure 8B-iii); and, finally, incubation of the surface with the antibody led to a significant decrease in current, due to detection of HIgG at the conjugation concentration (100 ng $mL^{-1}$; Figure 8B-iv).

The main characteristics of the detection capacity of a BioFET device is its inherent sensitivity to surface charge or surface potential, which can be quantified by the transistor gain or transconductance. Thus, the gain performance of a BioFET in solution can be quantified by replacing the gate voltage in the traditional transistor Gain definition Equation (2), with $V_{ref}$, which yields:

$$g_m = dI_{DS} / dV_{ref} \quad (2)$$

Figure 8C shows the transconductance for each of the aforementioned functionalization steps. The transconductance of the fully functionalized BioFET at HIgG (Figure 8B-iv) detection was lower than that of the bare BioFET (Figure 8B-i). Considering the lower capacitance in the BSA-functionalized EIS structure compared to that of the functionalized EIS (as shown in Section 3.1), the reduction in $g_m$ can be attributed to the changes in the effective capacitance due to the addition of organic layers, which by extension, applies to the BioFET.[49]

As mentioned previously, the main limitation of the BioFET has been found to be the detection limit level of around micrograms per milliliter. In this work we present a flexible BioFET capable of detecting 100 ng $mL^{-1}$ (1.5 nM) with a relative standard deviation (RSD) of 9% for BSA detection. Other works[50,51] employ fluoropolymers such as perfluor-1–3-dimethylcyclohexam (PFDMCH) and cyclic transparent optical fluoropolymer (CYTOP) or inorganic copper phthalacyanine (CuPc) as a top insulators. Fluoropolymers are good candidates to withstand wet environment and also do not suffer from hysteresis during bias stress, etc. Despite of higher sensitivity, the main challenge of these materials is the subsequent functionalization, due to the high hydrophobicity of the materials, without using expensive and sophisticate techniques such as plasma-enhanced chemical vapor deposition (PECVD), thermal evaporation, etc.; Table S7 (in the SI) shows a comparison of the mentioned works. Therefore, it remains desirable to develop: i) biosensors based on alternative top insulator materials, such as copolymer MMAcoMAA where these limitations are lessened,

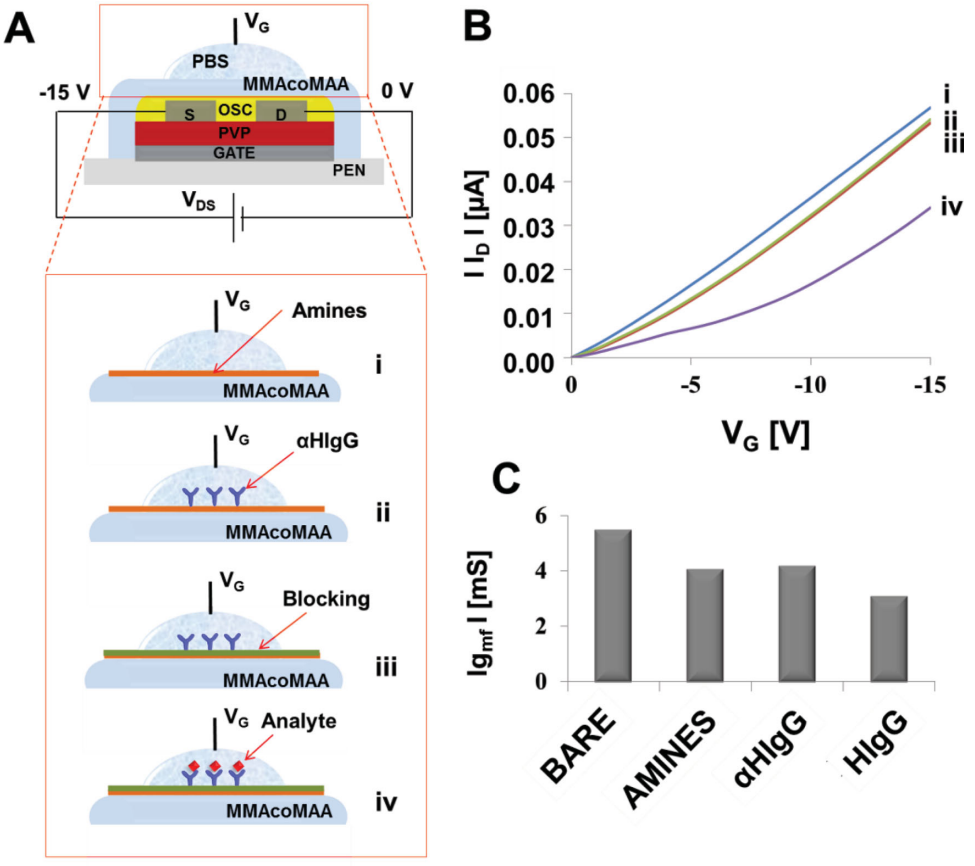


**Figure 8.** A) Schematic of the stepwise functionalization of the insulator (MMAcoMAA) in the BioFET: i) amino-functionalization (with 1% APTES); ii) immobilization of capture antibodies; iii) blocking to prevent non-specific absorption; and, iv) analyte conjugation. B) Corresponding current normalized transfer-curve plots for the MMAcoMAA BioFET gate after each of the conjugation steps. C) Transconductance (transistor gain) for each functionalization step.

and, ii) biosensors onto flexible substrate benefiting from low-temperature organic semiconductors unlike of the rigid silicon substrates. To the best of our knowledge, this work joins organic materials, flexible substrates and finally low-cost fabrication thanks to inkjet printing technology providing in this way a proof-of-concept of a label-free BioFET easily scalable to mass production and accessible for low-resource places/countries.

## 4. Conclusion

A fully integrated organic BioFET was designed, fabricated and tested for label-free protein detection. It was made by inkjet printing of an OFET and subsequent functionalization of the insulator with specific antibodies. Several constituent materials and operational configurations for the OFET and the final BioFET were evaluated electrically. Moreover, different materials and thicknesses for the insulator layer were assessed by insulator rupture evaluation. Both cPVP (for the bottom OFET) and MMAcoMAA (for the top BioFET) were validated as good insulators in the studied range of voltages.

Biofunctionalization of the MMAcoMAA surface, and selective adhesion of target proteins to the BioFET, were studied by colorimetric, fluorescence measurements and AFM images. For preliminary studies, an EIS structure was used to detect the protein BSA by *C*–*V* measurements. The repeatability was studied with different devices. Confocal and interferometry images were taken to assess the roughness of functionalized and immobilized protein structures. Finally, as proof of concept, the BioFET platform was tested for detection of the model protein HIgG (at a fixed concentration of 100 ng $mL^{-1}$).

The BioFET reported here represents an important starting point for the design and fabrication of flexible, organic biosensing devices by inkjet printing. Nevertheless, certain issues with such devices remain to be improved, including reproducibility in the fabrication process (in terms of achieving greater sensitivity and therefore, a lower limit of detection), the development of functional inks and extension of this technology to a wider array of substrates. The authors are confident that once this technology has matured, it will be amenable to miniaturization for integration into a fully functional device for point-of-care diagnosis.

## 5. Experimental Section

### 5.1. Materials and Instrumentation

*Reagents*: The transistor layers were deposited using with different inks. For the gate, drain, and source electrodes, silver nanoparticle solution (20% weight, EMD5603, Sunchemical Inc.; UK) dispersed in ethanol and ethanediol solvent was used. It was filtered using a nylon

based filter with a pore size of 0.45 µm. The bottom insulator material was cross-linked poly-4-vinylphenol (cPVP; $\bar{M}_w$ = 25 000; Sigma Aldrich, Spain) and solved in propylene glycol monomethyl ether acetate (PGMEA, Sigma Aldrich, Spain). The resulting solution was stirred for 30 min and, to obtain cPVP with the desired physical properties for jetting, it was subsequently filtered by a polytetrafluoroethylene (PTFE) 0.2 µm filter. The top insulator was based on methyl methacrylate copolymer (based on 9 wt% methyl methacrylate and 8.5 wt% methacrylic acid in ethyl lactate as solvent, named MMAcoMAA 8.5 EL9; MicroChem, Spain). The active channel was fabricated using an amorphous, polymeric *p*-type semiconductor (FS0027, FlexInk Inc.; UK) and tetralin as solvent. The filters were Whatman type (0.2 µm, Millipore, Spain). The substrate was a flexible polyethylene naphthalate (PEN) (Teonex® Q65FA; Dupont, Teijin,UK). Acid orange II dye; polystyrene microparticles (diameter: 1 µm, aq. solution, 10% solids, and density: $1 \times 10^{-05}$ g cm$^{-3}$); bovine serum albumin (BSA); BSA labeled with ALEXA 555 fluorophore; casein; (3-aminopropyl)triethoxysilane; capture antibody (goat anti-human IgG); Human IgG (analyte); ethyl(dimethylaminopropyl) carbodiimide (EDC); and *N*-hydroxysuccinimide (NHS) were all purchased from Sigma Aldrich, Spain.

*Instruments*: A Dimatix DMP2831 desktop printer (Fujifilm, USA) was used to print the layers. It employs one user-fillable, piezo-based inkjet print cartridge with 16 nozzles, able to jet droplets (1 or 10 pL) of diverse fluids with a variable jetting resolution. Drop-on-demand printing was performed in a class 10 000 cleanroom. The printer includes an alignment system to prevent layer misalignment when the sample is moved for curing processes or for changing the cartridge. Electrical measurements were performed using a B1500A semiconductor analyzer and E4980A LCR meter (both: Agilent, USA). Finally, a Süss Microtec EP 6 probe station is used as a tested for device characterization.

### 5.2. Optimization of the Insulator Layer

In order to choose an insulator material that would be biocompatible and would not compromise the performance of the BioFET, different insulators were tested using an MIE structure based on capacitance measurements. The MIE structure comprised (from bottom to top): a conductive layer; a spin-coated insulator layer; a drop of electrolyte (acetate buffer pH 4.0 + PBS pH 7.4; total volume: 2 µL); and finally, a reference electrode (Pt wire; diameter: 0.2 mm). Each of the following materials was separately evaluated as insulator: NOA 68 (adhesive), polyester resin, cPVP, and MMAcoMAA. The external reference electrode was used to perform electrical measurements to study the leakage current through the insulator. The measurements included *I*–*V* curves, and parallel capacitance ($C_p$) and resistance ($R_p$) at 1 KHz.

Additionally, each layer was studied for morphology and thickness measurements by scanning electron microscopy (SEM), using a Magellan microscope (FEI, USA).

### 5.3. Fabrication of the BioFET

A BioFET comprising (from bottom to top): a bottom gate (silver nanoparticle ink); a bottom insulator (cPVP); source and drain electrodes (silver nanoparticle ink); a *p*-type organic polymer semiconductor (FS-0027); a top insulator (MMAcoMAA); and a reference electrode (Pt wire) in contact with the electrolyte. These technical specifications of each ink and the fabrication process are described in Tables S1–4 in the SI.

*Deposition of the Bottom Gate*: Prior to printing, the substrate (PEN foil 125 µm thickness) was cleaned with ethanol for a few seconds, and then dried under nitrogen to remove any remaining particles. The bottom gate was deposited onto the substrate by inkjet printing of a silver nanoparticle solution. The cartridge and platen temperature were set at room temperature and 40 °C respectively. Drop spacing of 20 µm by using a 10 pL cartridge was established, and the jetting frequency and voltage was 10 KHz and around 22–23 V each. The resulting layer (average thickness: ca. 573 nm) was sintered at 130 °C for 30 min in a convection oven (Figure S6A and Table S1 in the SI).

*Deposition of the Bottom Insulator*: Cross-linked PVP (cPVP) was prepared by dissolving PVP in PGMEA at room temperature. The resulting solution was stirred for 30 min and, to obtain cPVP with the desired physical properties for jetting, it was subsequently filtered. The bottom insulator was deposited by inkjet printing of the previously prepared cPVP solution at room temperature (cartridge and platen), with a drop spacing of 20 µm by using a 10 pL cartridge, being the jetting frequency and voltage 10 KHz and around 23–26 V respectively. The resulting layer was baked at 200 °C for 20 min (final thickness: ca. 650 nm; Figure S6B and Table S2 in the SI).

*Deposition of the Source and Drain Electrodes*: Interestingly, silver can be printed directly onto cPVP; no surface pre-treatment is required. Thus, the source and drain electrodes were deposited directly onto the bottom insulator using the same silver nanoparticle ink, printing conditions and post-printing procedure as for the bottom gate (Figure S6C).

*Deposition of the Semiconductor*: Before deposition of the semiconductor, the source and drain electrodes layer were plasma-treated ($O_2$, 60%, 25 W) for 30 s, and then cured on a hot plate for 15 min at 120 °C (Figure S6D). The semiconductor layer was deposited onto the plasma-treated layer by inkjet printing of the amorphous *p*-type polymer FS0027, at room temperature (cartridge and platen), with a drop spacing of 25 µm by using a 10 pL cartridge. The jetting frequency and voltage was 10 KHz and around 12–14 V each (Figure S6D and Table S3 in the SI).

*Deposition of the Top Insulator*: The top insulator, comprising MMAcoMAA was deposited on top of the semiconductor layer by spin-coating it onto the substrate, and then baking the resulting device at 150 °C for 90 s on a hot plate (Figure S6E). The thickness of the MMAcoMAA insulator layer was controlled by two spin-coating steps, the first one in order to spread the material onto the device at 750 rpm for 10 s, and the second one to obtain the final thickness (1.5 µm) at 1500 rpm for 30 s. The layer was characterized and optimized by SEM. The insulator breakdown and the semiconductor/insulator interface were characterized by electrical measurements. (Figure S6E and Table S4 in the SI). Finally, regarding the jetting properties, examples of the waveform and the printability of the Sunchemical silver ink, FS0027 organic semiconductor, and cPVP are shown in SI. For the silver ink, the waveform shown in Figure S7A that generates stable and qualitative drop ejection has been used. The maximum jetting voltage was in the range of 22–29 V and the jetting frequency was set to 10 kHz. The perpendicular to the nozzle plate ejected drops exhibit a spherical shape which is an indicator for high quality materials deposition. For the semiconductor FS0027 the used waveform generates stable and good drop ejection. This w-shaped waveform leads to a stable drop formation of the organic semiconductor. The jettability of the organic semiconductors was very stable using the Dimatix 16 nozzles inert printheads. The droplets are ball-shaped and the drop ejection is perpendicular to the nozzle plate. In general, the ink can be used without problems in multi nozzle mode. (Figure S7B). Finally the waveform for the c-PVP ink was developed for stable drop ejection (Figure S7C).

*Addition of Electrolyte*: To enable operation of the BioFET in aqueous media for biosensing experiments, a drop of electrolyte solution (0.1 M freshly prepared PBS pH 7.4) was added to the top of the top insulator, for use as both electrolyte and incubation buffer.

### 5.4. Amino-Functionalization of the MMAcoMAA Insulator Surface

The surface of the MMAcoMAA insulator was functionalized to enable binding of the target protein. This entailed two main steps: *amino-functionalization* (described here), and *antibody attachment* (described below). The MMAcoMAA layer was plasma-oxidized, and then incubated with APTES. Different surface concentrations of amino groups were compared and characterized by quantitative colorimetry, using acid orange II dye. This method comprised immersion of the substrate

with the amino-functionalized MMAcoMAA in an aqueous solution of acid orange II (the pH of the solution was adjusted to 3, using HCl 1 M). After shaking overnight at room temperature for at least 12 h, the samples were washed twice with the acid solution. In order to dissolve the adsorbed acid orange II, the samples were shaken for 15 min at room temperature in aqueous NaOH (pH 12). The concentration of dye (which was similar to the surface amino concentration of functionalized MMAcoMAA) in the solution was determined by absorbance measurements, using an optical spectrometer at 485 nm.[52]

Functionalization was confirmed by other methods, including fluorescence detection by using a fluorophore, immobilization of polystyrene microparticles, contact-angle studies, and AFM. In the first experiment, the BSA-ALEXA 555, containing 1:1 EDC/NHS, was added dropwise onto two different MMAcoMAA surfaces (either bare or amino-functionalized) for 2 h. The resulting MMAcoMAA surfaces were then cleaned with PBST, blocked with the blocking buffer (described in the experimental part), washed again with PBST, and, finally, subjected to fluorescence measurements. Another simple test used to confirm the surface functionalization with amino groups was the immobilization of polystyrene microparticles. The microparticle solution was added dropwise to each of two surfaces (bare or amino-functionalized), which were then incubated for 15 min and, finally, washed with PBST. Polystyrene microparticles remained bound to the functionalized surface, but were washed off from the unfunctionalized surface by PBST (Figure S4). Finally, complementary studies were realized by using AFM as well as angle contact (Figure S5).

### 5.5. Attachment of Antibodies to the Amino-Functionalized MMAcoMAA Insulator Surface

Once the amino-functionalization of the MMAcoMAA surface had been optimized, specific antibodies were attached to the surface amino groups. To this end, 15 µL of goat anti-human IgG (0.5 mg $mL^{-1}$) were covalently bound to the amino groups through peptide coupling, using 135 µL of a solution of 1:1 EDC/NHS in PBS (5 mg $mL^{-1}$) at room temperature for 30 min. The resulting surface was then washed with PBST. The free sites on the antibody-functionalized surface were then blocked, using PBS supplemented with 5% (w/v) casein and 0.005% (v/v) Tween 20 for 30 min. Finally, the blocked, functionalized surface was washed with PBST.

### 5.6. Label-Free Protein Detection

As proof-of-concept, the final BioFET was evaluated for label-free detection of Human IgG, used as model protein. Human IgG was drop-casted onto the blocked, antibody-functionalized surface of the BioFET. The system was incubated for 30 min and finally, washed with PBST to remove any excess analyte. The amount of Human IgG bound to the BioFET was quantified by *I–V* measurements.

## Supporting Information

Supporting Information is available from the Wiley Online Library or from the author.

## Acknowledgements

The authors thank the MICINN (projects MAT2011–25870 and TEC2011–29800) and the European Commission (FP7 project NADINE [contract # 246513]) for funding the research presented here. Fulvia Villani from ENEA center, Naples (Italy), for the study of the roughness and viscosity of the used materials, and Enrico Sowade and Kalyan Yoti from Digital Printing and Imaging Technologies, Chemnitz, Germany, for the printer waveforms are acknowledged. The authors are also grateful for the technical support given by Ana Alcalde-Aragonés for the BioFET fabrication, and Dámaso Torres for the 3D schematic images of the BioFET, including the cover proposal.

Received: April 12, 2014
Revised: June 8, 2014
Published online: July 31, 2014

[1] T. Sekitani, T. Yokota, U. Zschieschang, H. Klauk, S. Bauer, K. Takeauchi, M. Takamiya, T. Sakurai, T. Someya, *Science* **2009**, *326*, 1516.
[2] A. Facchetti, *Chem. Mater.* **2011**, *23*, 733.
[3] D. Gentili, P. Sonar, F. Liscio, T. Cramer, L. Ferlauto, F. Leonardi, S. Milita, A. Dobabalapur, M. Cavallini, *Nano Lett.* **2013**, *13*, 3643.
[4] A. N. Sokolov, M. E. Roberts, Z. Bao, *Mater. Today* **2009**, *12*, 12.
[5] L. Caizhi, F. Yan, *Polym. Rev.* **2013**, *53*, 352.
[6] J. Lu, K. S. Moon, C. P. Wong, *IEEE Proc. of the Electronic Components and Technology Conference*, **2007**, *57*th, p. 453.
[7] C. W. Wang, C. Y. Pan, H. C. Wu, P. Y. Shih, C. C. Tsai, K. T. Liao, L. L. Lu, W. H. Hsieh, C. D. Chen, Y. T. Chen, *Small* **2007**, *3*, 1350.
[8] E. Stern, A. Vacic, N. K. Rajan, J. M. Criscione, J. Park, B. R. Ilic, D. J. Mooney, M. A. Reed, T. M. Fahmy, *Nat. Nanotechnol.* **2010**, *5*, 138.
[9] H. U. Khan, M. E. Roberts, W. Knoll, Z. Bao, *Chem. Mater.* **2011**, *23*, 1946.
[10] D. Sarkar, W. Liu, X. Xie, A. C. Anselmo, S. Mitragotri, K. Banerjee, *ACS Nano.* **2014**, *8*, 3992.
[11] B. A. Ridley, B. Nivi, J. M. Jacobson. *Science* **1999**, *286*, 746.
[12] M. Zhanga, P. Lina, M. Yang, F. Yan, *Biochim. Biophys. Acta* **2013**, *1830*, 4402.
[13] L. Kergoat, B. Piro, M. Berggren, G. Horowitz, M.-Ch. Pham, *Anal. Bioanal. Chem.* **2012***402*, 1813.
[14] C. R. Newman, C. D. Frisbie, D. A. da Silva Filh, J. L. Brédas, P. C. Ewbank, K. R. Mann, *Chem. Mater.* **2004**, *16*, 4436.
[15] M. J. Schöning, A. Poghossian, *Analyst* **2002**, *127*, 1137.
[16] D. Elkington, N. Cooling, W. Belcher, P. C. Dastoor, X. Zhou, *Electronics* **2014**, *3*, 234.
[17] G. C. Jensen, C. E. Krause, G. A. Sotzingab, J. F. Rusling, *Phys. Chem. Chem. Phys.* **2011**, *13*, 4888.
[18] N. Y. Shim, D. A. Bernards, D. J. Macaya, J. A. DeFranco, M. Nikolou, R. M. Owens, G. G. Malliara, *Sensors* **2009**, *9*, 9896.
[19] Y. Wen, Y. Liu, Y. Guo, G. Yu, W. Hu, *Chem. Rev.* **2011**, *111*, 3358.
[20] M. C. Dang, T. M. D. Dang, E. Fribourg-Blanc, *Adv. Nat. Sci.: Nanosci. Nanotechnol.* **2003**, *4*, 015009.
[21] M. Tudorache, C. Bala, *Anal. Bioanal. Chem.* **2007**, *388*, 565.
[22] S. A. Ruiz, C. S. Chen, *OFT Matter* **2007**, *3*, 1.
[23] X. Liu, J. T. Guthrie, *Surface Coatings Int. Part B* **2003**, *86*, 91.
[24] W.-K. Lee, P. E. Sheehan, *Scanning* **2008**, *30*, 172.
[25] M. Singh, H. M. Haverinen, P. Dhagat, G. E. Jabbour, *Adv. Mater.* **2010**, *22*, 673.
[26] A. K. Yetisen, M. S. Akram, C. R. Low, *Lab Chip* **2013**, *13*, 2210.
[27] A. P. F. Turner, *Chem. Soc. Rev.* **2013**, *42*, 3184.
[28] H. Jeong, N. Erdene, J. H. Park, D. H. Jeong, S. K. Lee, *Biosens. Bioelectron.* **2013**, 346.
[29] R. Li, H. Yu, Y. Li, R. Feng, X. Li, H. Li, Q. Wei, B. Du, *Anal. Methods* **2013**, *5*, 5534
[30] T. Li, E-J. Jo, M-G. Kim, *Chem. Commun.* **2012**, *48*, 2304.
[31] R. D. Nargessi, B. Shine, L. Landon, *J. Immuno. Methods* **1984**, *71*, 17.
[32] H. V. Aboul-Enei, RI. Stefan, S. Litescu, G. L. Radu, *J. Immunoassay Immunochem.* **2002**, *23*, 181.
[33] J. Li, J-J. Zhu, *Analyst* **2013**, *138*, 2506.

[34] J. A. Lim, W. H. Lee, H. S. Lee, J. H. Lee, Y. D. Park, K. Cho, *Adv. Funct. Mater.* **2010**, *18*, 229.
[35] R. D. Deegan, O. Bakajin, T. F. Dupont, G. Huber, R. Nagel, T. A. Witten. *Nature* **1997**, *389*, 827.
[36] E. Ramon, C. Martínez-Domingo, J. Carrabina, *J. Imaging Sci. Technol.* **2013**, *57*, 40402.
[37] Z.-J. Jiang, C.-Y. Liu, L.-W. Sun, *J. Phys. Chem.* **2005**, *109*, 1730.
[38] P. Vicca, S. Steudel, S. Smout, A. Raats, J. Genoe, P. Heremans, *Thin Solid Films* **2010**, *519*, 391.
[39] Y. Guo, G. Yu, Y. Liu, *Adv. Mater.* **2010**, *22*, 4427.
[40] I. Bae, J. Kang, Y. J. Hin, Y. J. Park, R. H. Kim, F. Mathevet, C. Park, *Adv. Mater.* **2011**, *23*, 3398.
[41] M.-B. Madec, P. J. Smith, A. Malandraki, N. Wang, J. G. Korvink, S. G. Yeates, *J. Mater. Chem.* **2010**, *20*, 9155.
[42] S. Y. Cho, J. M. Ko, J. Lim, J. Y. Lee, C. Lee. *J. Mater. Chem. C* **2013**, *1*, 914.
[43] X. Cheng, M. Caironi, Y. Y. Noh, J. Wang, C. Newman, H. Yan, A. Facchetti, H. Sirringhaus, *Chem. Mater.* **2010**, *22*, 1559.
[44] J.-H. Bae, H. Kim, G. Horowitz, S. D. Lee, *Solid-State Electron.* **2011**, *63*, 163.
[45] I. Bae, J. Kang in, Y. J. Park, R. H. Kim, F. Mathevet, C. Park, *Adv. Mater.* **2011**, *23*, 3398.
[46] A. Jedaa, M. Halik, *Appl. Phys. Lett.* **2009**, *95*, 103309.
[47] F. Werkmeister, B. Nickel. *J. Mater. Chem. B* **2013**, *1*, 3830.
[48] A. Tataroglu, S. Altindal, *Microelectron. Eng.* **2006**, *83*, 582.
[49] B. Khamaisi, O. Vaknin, O. Shaya, N. Ashkenasy, *ACS Nano* **2010**, *8*, 4601.
[50] H. U Khan, J. Jang, J. J. Kim, W. Knoll, *Biosens. Bioelectron.* **2011**, *26*, 4217.
[51] W. Huang, K. Besar, R. LeCover, P. Dulloor, J. Sinha, J. F. M. Hardigree, H. E. Katz, *Chem. Sci.* **2014**, *5*, 416.
[52] E. Uchida, Y. Uyama, Y. Ikada, *Langmuir* **1993**, *9*, 1121.